



PERGAMON

Journal of the Mechanics and Physics of Solids  
50 (2002) 2333–2353

---

---

JOURNAL OF THE  
MECHANICS AND  
PHYSICS OF SOLIDS

---

---

[www.elsevier.com/locate/jmps](http://www.elsevier.com/locate/jmps)

# Electrically driven cracks in piezoelectric ceramics: experiments and fracture mechanics analysis

S.L. dos Santos e Lucato<sup>a</sup>, H.-A. Bahr<sup>b</sup>, V.-B. Pham<sup>b</sup>,  
D.C. Lupascu<sup>a</sup>, H. Balke<sup>b</sup>, J. Rödel<sup>a,\*</sup>, U. Bahr<sup>c</sup>

<sup>a</sup>*Darmstadt University of Technology, Institute of Materials Science, Ceramics Group, Petersenstr. 23, 64287 Darmstadt, Germany*

<sup>b</sup>*Dresden University of Technology, Institute of Solid Mechanics, 01062 Dresden, Germany*

<sup>c</sup>*Dresden University of Technology, Institute of Theoretical Physics, 01062 Dresden, Germany*

Received 22 October 2001; received in revised form 26 March 2002; accepted 4 May 2002

---

## Abstract

Piezoelectric systems like multilayer actuators are susceptible to damage by crack propagation induced by strain incompatibilities. These can arise under electric fields for example between the electroded and external regions. Such incompatibilities have been realised in thin rectangular model specimens from PZT-piezoelectric ceramics with top and bottom electrodes only close to one edge. Under an electric field, controlled crack propagation has been observed in situ in an optical microscope. The crack paths are reproducible with very high accuracy. Small electrode widths lead to straight cracks with two transitions between stable and unstable crack growth regions, while large electrode widths result in curved cracks with four transitions. Fracture mechanics analysis is able to explain the different crack paths. An iteration method is developed to simulate the curved crack propagation also for strong curvature of the crack paths using the finite element method. The computed crack contours exhibit excellent quantitative agreement with the experiment with respect to their shape, the stages of stable and unstable crack propagation and the transitions between them. Finally, also the crack length as a function of the electric field can be predicted. © 2002 Elsevier Science Ltd. All rights reserved.

*Keywords:* A. Crack propagation and arrest; A. Delamination; B. Piezoelectric material; B. Strain compatibility; C. Finite elements

---

---

\* Corresponding author. Tel.: +49-6151-166316; fax: +49-6151-166314.  
E-mail address: [roedel@ceramics.tu-darmstadt.de](mailto:roedel@ceramics.tu-darmstadt.de) (J. Rödel).

## 1. Introduction

Ceramic actuators are used for numerous applications such as high-frequency, low-amplitude devices in adaptive structures and vibration control (Uchino, 1997; Haertling, 1999). Respective components have been accepted in the aircraft and automobile industry as well as in printing and textile machinery. Albeit exhibiting some ferroelastic toughening, the fracture toughness of ferroelectric actuator materials is rather small and thus, they are susceptible to fracture under high electric fields or mechanical stresses. Therefore, the limited reliability of the component due to cracking constitutes a major impediment to large-scale usage.

The most cost-efficient geometry for such actuators is that of the cofired multilayer actuator. The common design consists of two interdigitating electrodes carrying the disadvantage of electrodes ending inside the ceramic. As a consequence, the ceramic material, which exhibits ferroelectric and ferroelastic as well as piezoelectric behaviour, experiences a strain incompatibility between the electrically inactive material regions and the electrically active material regions. A complex mechanical stress field centred at the electrode edge arises and can lead to crack initiation in this area, crack growth, and finally to the failure of the device.

Studies of the damage mechanisms in ceramic multilayer actuators made of piezoelectric materials have revealed that cracks are formed preferentially at the internal electrode edge (Aburatani et al., 1994; Furuta and Uchino, 1993). Takahashi et al. (1983) calculated the stress distribution around the electrode edge by means of a linear finite element method and showed that the magnitude of the tensile stresses is comparable to the strength of the ceramic. Further investigations on model and real actuators under cyclic bipolar and unipolar electric fields were performed by Schneider et al. (1995, 1996). It was shown that cracks are formed during the first few cycles. In an earlier work, we have investigated crack initiation at the first poling cycle and could show that a large number of cracks are formed at about the coercive field ( $E_C$ ) and grow with an increase of the electric field (dos Santos e Lucato et al., 2001).

In this work we analyse crack growth at the first poling cycle in a model geometry. Thin rectangular specimens with top and bottom electrodes only on one side and a pre-crack were used as shown in Fig. 1. If an electric field is applied between the two electrodes, the material will contract in the directions perpendicular to the field and expand in the direction of the applied electric field. As the adjacent material is not affected by the electric field it will mechanically clamp the active strip. A strain mismatch is induced and high stresses arise leading to crack growth. In order to focus solely on crack growth, a pre-crack is artificially introduced.

Thin specimens have been chosen to obtain through-thickness cracks with equal lengths on the top and bottom side so that cracking can be analysed by means of fracture mechanics using a two-dimensional finite element model. An iteration method is developed to simulate the curved crack-propagation also for strong curvature of the crack paths. For the quantitative fracture mechanics analysis, experimental data of fracture toughness and incompatible strains (consisting of ferroelectric, ferroelastic and piezoelectric strain) as driving force for the cracks are needed.

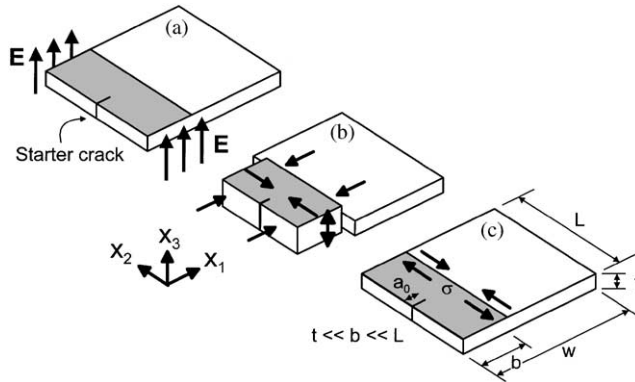


Fig. 1. Stress generation by mechanical clamping due to partial electrode coverage. (a) Electric field is applied on the electrodes (active material). (b) Shrinkage in  $x_1$  and  $x_2$  directions and expansion in  $x_3$  direction of the active part ensues. (c) Adjacent material mechanically clamps the active strip and high tensile stresses arise.

## 2. Experimental methods

All experiments were performed on a commercial lead zirconate titanate, PIC 151 (PI Ceramics, Lederhose, Germany). The specimens were delivered as plates of dimensions  $40 \times 40 \text{ mm}^2$  with thicknesses of 0.5 and 1 mm. They were polished on one side to a  $1 \mu\text{m}$  finish. Due to different polishing times for the different specimens, a small variation of the final thicknesses was obtained. Electrically driven crack-propagation measurements were performed. Additionally fracture data ( $R$ -curve) and displacements were measured providing inputs for the fracture mechanics analysis.

A co-ordinate system is used as follows. Direction  $x_3$  is the electric field direction,  $x_2$  is parallel to the electrode edge and  $x_1$  is perpendicular thereto forming a right-hand co-ordinate system (Fig. 1). The electrode coverage is defined by  $b/W$ , where  $b$  is the electrode width and  $W$  the specimen width. The volume between the electrodes will be defined as active material and the remainder inactive material. The length of the electrode is given by the length  $L = W$ .

### 2.1. $R$ -curve measurement

The  $R$ -curves were measured in the compact tension geometry. Plates with 0.5 mm thickness proved too fragile for mechanical loading. Therefore,  $R$ -curves were obtained using the 1 mm thick plates cut to compact tension specimens of  $35 \times 33.6 \text{ mm}^2$ . The test itself was performed based on ASTM 399 (1996) with some improvements. The CT testing device is a new version of the type used before (Rödel et al., 1990) and was mounted on a co-ordinate stage on an optical microscope. A computer with custom designed software connected to the stage is used to read out the stage co-ordinates and the applied load. The crack length was obtained by targeting the crack-tip with the crosshairs in the eye-pieces. With the crack length and applied load known, the

applied stress intensity factor and the crack growth velocity were calculated in real time by the data-acquisition software. The crack growth is maintained at a constant velocity throughout the whole measurement.

Prior to the *R*-curve measurement, a sharp pre-crack was produced using a half chevron notch and a Knoop indent with load of 50 N as described in Rödel et al. (1990). After the pre-crack had been driven through the region of the half chevron notch, it was then renotched to a final length of approx. 600  $\mu\text{m}$ . The end of the notch is used as origin for the crack extension  $\Delta a$ . To ensure maximum reproducibility, special care was taken to record data at crack velocities at about  $10^{-6}$  m/s. A data point was recorded every 25  $\mu\text{m}$  up to the final crack extension of about 5 mm.

## 2.2. Displacement measurement

The incompatible strains needed for the fracture mechanics analysis cannot be directly measured, but can be computed from displacements. Therefore, displacements were measured parallel to the electrode edge ( $x_2$ ) using specimens with 0.5 mm thickness. The preparation procedure was as follows. First electrodes of Au/Pd (80%/20%) were sputtered onto the 0.5 mm thick  $40 \times 40 \text{ mm}^2$  specimens. To achieve only partial coverage, stencils of overhead transparencies were cut and attached to both surfaces by superglue and removed after sputtering. The electrodes had a final thickness of approx. 50 nm. Two different electrode widths were prepared, namely 1 and 2 mm. A narrow strip of silver paint was applied along the centre of each electrode to ensure complete contact along the electrode length in all stages of cracking. Thin copper wires were glued parallel to the electrode edge on both electrodes using a conducting 2-component epoxy to connect both sides of the crack. One side of each copper wire extended beyond the specimen edge and served as connection to the high voltage source.

A linear variable displacement transducer (LVDT) with a very thin alumina tip was used as shown in Fig. 2. In case of the partially electroded specimens, the tips of the LVDT and the ground fixture were very carefully placed 0.5 mm from the specimen edge on the side specimen faces. Silicone oil with a molecular weight of 1000 was applied to the electrodes for electric insulation. A field of 2 kV/mm (approx.  $2E_C$ ) was then applied at a rate of 12.5 V/mm s for the displacement measurement. The data was logged with a rate of 50 points per second.

A second set of displacement measurements was performed with fully electroded specimens of  $20 \times 20 \text{ mm}^2$ . The copper wires were attached in the centre of each electrode while the LVDT tips were mounted on the centre of the side surfaces and the applied electric field was increased up to 4 kV/mm. In order to prevent arcing at these high fields, the specimens were placed in a cup filled with Flourinert<sup>®</sup> 77 (3M Corporation). The field ramp and the data logging was done with the same rate as the first measurement set. Each set of displacements was obtained on two specimens.

## 2.3. Crack propagation under electric field

The specimen preparation for the crack propagation under electric field measurements was the same as for the displacement measurements but additional steps were needed. A

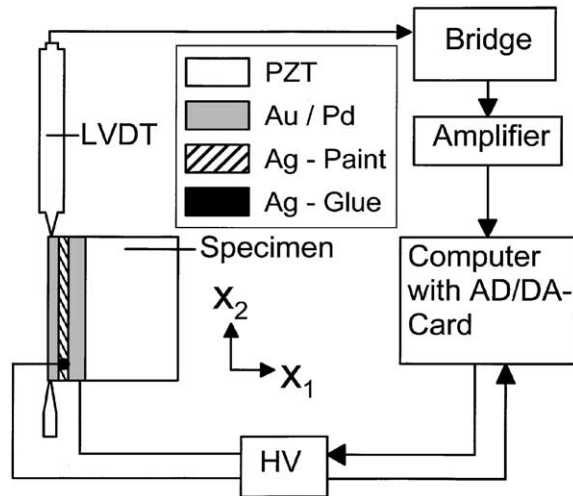


Fig. 2. Experimental set-up to measure the displacement hysteresis loop.

pre-crack was introduced by placing a Knoop-indent onto the front specimen face. The specimen was clamped in upright position by a high-precision wrench and the indent was placed using a load between 30 and 50 N for 10 s depending on the desired crack length. Finally, the elastic–plastic contact zone with the attendant residual stress zone was sanded away using alumina paper. A sharp pre-crack extending from top to bottom electrode is obtained.

The pre-cracked specimens were placed in a holding fixture filled with Flourinert<sup>®</sup> 77 for electric insulation. The fixture was mounted onto the co-ordinate stage in the optical microscope and a high-voltage source was connected to the specimen. A computer with an AD/DA-card was used to control the HV-source. In the measuring cycle the voltage applied to the specimen was increased by steps of 68 V/mm at a ramp of 12.5 V/mm s. After waiting for approx. 30 s the crack-tip was targeted with the crosshairs in the eye-pieces of the optical microscope and the co-ordinates were transferred to a custom designed CAD-type software. The waiting time was inserted to let the crack grow subcritical to a very low velocity and, therefore maintain uniform conditions for all data points. The increment-measurement cycle was repeated until the active material saturated and no further crack growth was observed. Two specimens with thicknesses of 0.51 and 0.31 mm were used in case of an electrode width of 2 mm (1.95 and 1.87 mm exactly) and one specimen with a thickness of 0.44 mm was used for the 1 mm (1.07 mm exactly) electrode.

### 3. Experimental results

#### 3.1. *R*-curve

As the crack has not been renetched to small lengths and the specimen was not thermally depolarised after growing the starter crack, the initial value of the *R*-curve could

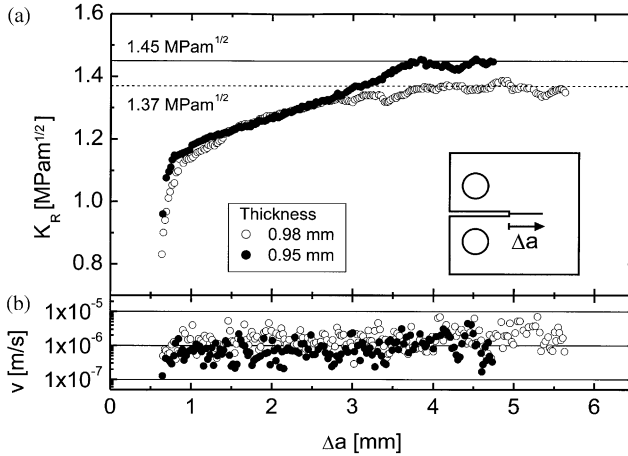


Fig. 3. (a)  $R$ -curve for unpoled material; (b) corresponding crack growth velocity.

not be measured with high precision. The  $R$ -curves start at about  $0.8\text{--}0.9 \text{ MPa m}^{1/2}$  in Fig. 3. A steep rise up to  $1.15 \text{ MPa m}^{1/2}$  is observed in the first  $500 \mu\text{m}$  of crack extension. It changes into a linear increase of the fracture toughness up to an extension of about  $3.5 \text{ mm}$  after which the fracture toughness remains constant. These final toughness values are termed plateau values and range from  $1.37$  to  $1.45 \text{ MPa m}^{1/2}$ . The  $R$ -curves and the corresponding crack growth velocity are shown in Fig. 3. The crack growth velocity was maintained at about  $10^{-6} \text{ m/s}$  with deviations of less than a factor of 3.

### 3.2. Measured displacements

The measured displacements for the different geometries are shown in Fig. 4. Beneath the electrode edges in the specimen, electric field singularities occur which give rise to high localised stresses and cracking (small cracks) (dos Santos e Lucato et al., 2001). It is assumed that these small cracks do not essentially affect the measured global displacements and the global field distributions. Therefore, they are not considered in the measurements and in the theoretical analysis (Section 5). At a field of  $1.8\text{--}1.9 \text{ kV/mm}$  one of the many cracks formed at the internal electrode edge grew unstable to the external electrode edge (as indicated in Fig. 4). As the electroded side of the specimen is now divided, the displacements on the outer sides where the LVDTs are mounted are reduced. In the fully covered specimens no cracking was obtained and therefore the displacements could be measured up to the maximum field of  $4 \text{ kV/mm}$ . The maximum displacement before the crack appeared in the partially electroded specimens is about  $-30.6 \pm 2.6 \mu\text{m}$ . At the maximum electric field a displacement of  $-49.1 \pm 1.1 \mu\text{m}$  was obtained from the fully electroded specimens.

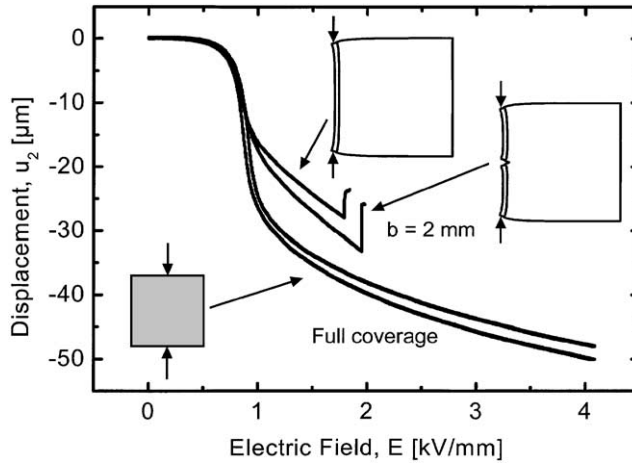


Fig. 4. Displacements under clamped conditions ( $40 \times 40 \text{ mm}^2$  with  $b = 2 \text{ mm}$ ) and in the free specimen ( $20 \times 20 \text{ mm}^2$ ).

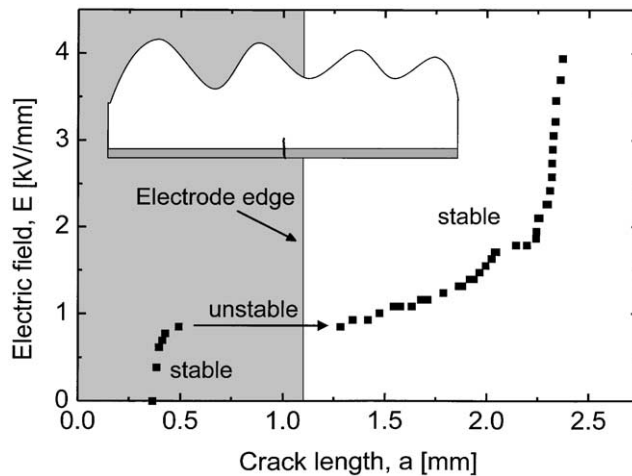


Fig. 5. Measured crack length as a function of the electric field for the straight crack. Note two transitions between stable and unstable crack propagation. The crack path as observed in the optical microscope is shown in the insert.

### 3.3. Crack mapping

#### 3.3.1. Straight crack propagation

Two different crack shapes can be identified. In the case of a 1 mm wide electrode a straight crack propagating perpendicular to the electrode edge is observed in Fig. 5. A starter crack of 0.36 mm was obtained after removal of the indent. An increase of

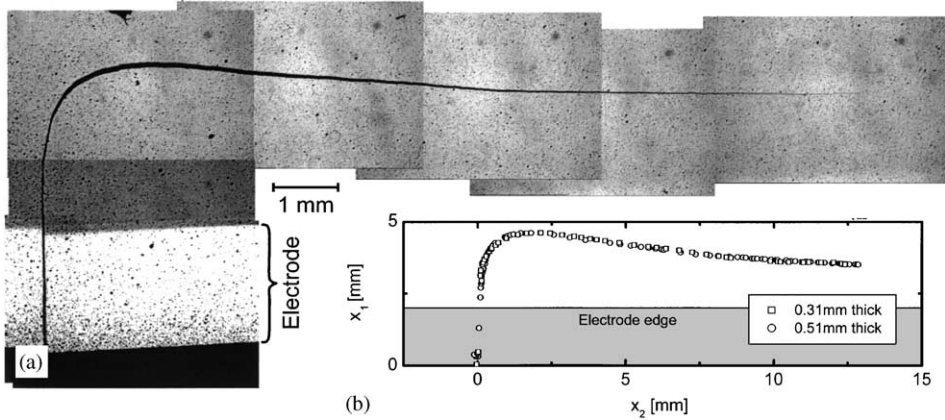


Fig. 6. (a) Photo of final crack configuration for a curved crack; (b) Comparison of two different experiments with curved cracks with specimens of different thicknesses.

electric field prompted crack propagation in the  $x_1$ -direction perpendicular to the electrode edge. Crack growth was first observed at a field of 0.38 kV/mm and remained stable up to a crack length of 0.49 mm at 0.85 kV/mm (Fig. 5). Unstable crack propagation across the electrode edge followed and produced a crack of length of 1.28 mm. Further increase of the electric field lead to stable crack growth up to a field of 3.94 kV/mm at which no further crack growth was observed as the strain between the electrodes saturated. The final crack length was 2.37 mm. Fig. 5 displays the crack length and the electric field needed to achieve this length. The insert provides the crack pattern as measured in the optical microscope.

### 3.3.2. Curved crack propagation

A curved crack starting perpendicular to the electrode edge and turning parallel to the electrode edge is obtained for an electrode width of 2 mm (Fig. 6a). The shapes of the cracks in the two specimens are identical (Fig. 6b). A straight crack is observed for the first 3 mm of crack growth. The crack then begins to curve towards the new direction parallel to the electrode edge. At a length of approx. 7 mm the crack had turned by  $95^\circ$  and continued to grow almost parallel to the electrode edge. The crack length is taken as the full length following the curvature of the crack as indicated in the insert in Fig. 7.

The crack-length vs. electric field data was obtained for two specimens (Fig. 7). A starter crack of 0.56 mm was introduced in the first specimen of 0.31 mm thickness. First crack propagation was observed at an electric field of 0.65 kV/mm and the crack growth was stable up to a field of 0.97 kV/mm at which the crack had a length of 0.59 mm. Unstable crack growth followed and the crack arrested at a length of 3.25 mm. A second region of stable crack growth, exhibiting an almost linear relationship of crack length and electric field up to a field of 2.13 kV/mm and a crack length of 4.59 mm is observed. Again, a second region of unstable crack growth sets in. The crack arrested

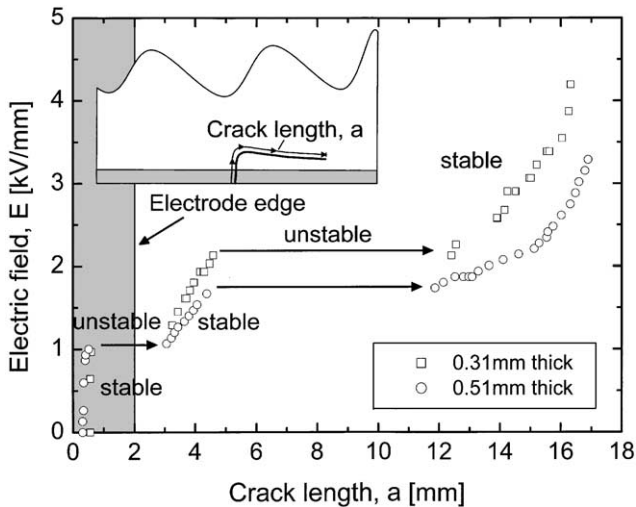


Fig. 7. Measured crack length as a function of the electric field for the curved crack. Note four transitions between stable and unstable crack propagation. The crack path as observed in the optical microscope is shown in the insert.

at a length of 12.41 mm and continued to grow stable until the specimen saturated at a field of 4.19 kV/mm and a final crack length of 16.33 mm.

The second specimen had a thickness of 0.51 mm and a starter crack of 0.31 mm. The first stable crack growth region extended from a field of 0.13 kV/mm to a field of 1.00 kV/mm corresponding to a crack length of 0.52 mm. The second stable region was obtained between the crack lengths of 3.05 and 4.37 mm which occurred at an electric field of 1.67 kV/mm. Finally, the last stable region is observed from 11.87 to 16.89 mm at which the specimen saturated at a field of 3.29 kV/mm.

#### 4. Qualitative fracture mechanics description

In this section, salient aspects of the different crack propagation regimes observed above will be discussed using some simplifying idealisations: A semi-infinite specimen exhibits a constant stress  $\sigma$  in the electrode region due to strain incompatibility. Furthermore, the material parameters remain identical for both active and inactive zones and quasi-static fields. Under these assumptions, the quasi-static squared stress intensity factor can be sketched qualitatively in Fig. 8 for two situations: a straight crack and a primary straight and then deflected crack with total crack length of  $a$ .

In this figure, for a constant electric field, i.e. constant  $\sigma$ , the squared stress intensity factor  $K_I^2$  increases linearly with crack length  $a$  in the electroded zone as an edge crack under constant stress ( $K_I^2 = 3.95\sigma^2 a$ ) and decreases outside of the electroded zone like an edge crack under point force for  $a \gg b$  ( $K_I^2 = 2.13\sigma^2 b^2/a$ ). Note that the asymptote for the straight crack is  $K_I^2 = 0$  and for the deflected crack  $K_I^2 = 0.343\sigma^2 b$  (Hutchinson

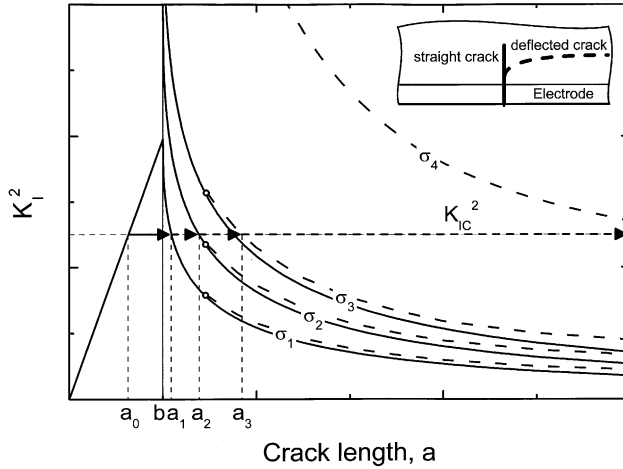


Fig. 8. Squared mode I stress intensity factor for a crack in a semi-infinite specimen for different  $\sigma$ . The full line denotes the straight crack in the symmetry and the dashed line the primary straight and then deflected crack (full arrow: unstable crack propagation; dashed arrows: stable crack propagation).

and Suo, 1992). It can be concluded that the  $K$ -curve for the deflected crack in the inactive region is always higher than for the straight crack (Fig. 8). Thus a long crack favours the deflected path because it can release more energy than on the straight path. Larger indices in Fig. 8 stand for increased  $\sigma$ , i.e. higher electric fields.

In our analysis, we apply linear-elastic fracture mechanics for a non-kinked crack which was always obtained in our experiments:

$$K_I \geq K_{Ic}, \quad K_{II} = 0. \tag{1}$$

Here,  $K_{Ic}$  is the critical stress intensity factor or the fracture toughness. The criterion of local symmetry for a non-kinked crack  $K_{II} = 0$  determines the curved crack path (Cotterell and Rice, 1980) and is automatically fulfilled by a straight crack on the symmetry line. Note that the dielectric displacement intensity factor  $K_{IV}$  (Suo et al., 1992) vanishes everywhere over the entire crack because in the electrode zone the electric field is parallel to the crack front due to symmetry arguments and zero in the inactive, unpoled zone.

A set of crack propagation scenarios is used to illustrate our problem with the aid of Fig. 8. An initial crack  $a_0 < b$  starts propagating unstable (full arrow) at a given  $\sigma_1$  satisfying conditions (1). This unstable stage will end at the crack length  $a_1$ , where the condition  $K_I = K_{Ic}$  is met at the downward slope of the  $K$ -curve for  $\sigma_1$ . Dynamic effects, which should drive the crack to a length  $a > a_1$ , are not considered. An increase of stress  $\sigma$  will prompt stable crack propagation under the condition  $K_I = K_{Ic}$  up to the crack length  $a_2$  at  $\sigma_2$  (dashed arrow). The crack path remains straight, as long as the bifurcation (open circle) point between straight crack (full line) and deflected crack (dashed line) in Fig. 8 remains below  $K_{Ic}^2$ . An increase of  $\sigma$  to  $\sigma_3$  moves this point above  $K_{Ic}^2$ . Therefore, the crack will deflect, as it can release more energy on

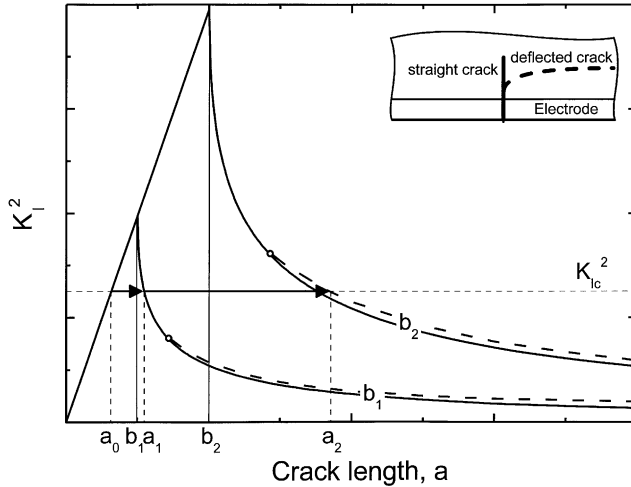


Fig. 9. Squared mode I stress intensity factor for a crack in a semi-infinite specimen by variation of the width  $b$ . The full line denotes the straight crack in the symmetry and the dashed line the primarily straight and then deflected crack (full arrow: unstable crack propagation).

the deflected path than on the straight one. It will continue growing stably until the  $K_I$ -asymptote reaches  $K_{Ic}$  at  $\sigma_4 = K_{Ic}/(0.343b)^{0.5}$ . Then it grows unstably again to an infinite crack length.

Please note that a perfectly straight crack in an entirely homogenous specimen remains straight. It can only deflect if a disturbance in the crack path or in the applied stresses is introduced. This is always the case in a polycrystalline material as ours because no crack runs exactly straight and local stress inhomogeneities due to pores, grain orientation, etc., are always present. For the above qualitative discussion we can assume that the crack has been artificially disturbed from its straight path at some point. Because the T-stress is positive in this model, the crack will not return to the straight path (Cotterell and Rice, 1980).

The different crack paths depending on the electrode width  $b$  are discussed by means of Fig. 9. Note that the bifurcation crack length corresponding to the open circle scales with  $b$  as the only characteristic length in this problem where the crack path follows from  $K_{II}=0$  (see 5.3). A small electrode width  $b$  ( $b_1$  in Fig. 9) favours a straight crack in the first unstable stage. The straight crack cannot turn (see Section 3.3.1), as long as the stress field cannot be further increased to reach the branching point in Fig. 9. In contrast, a large electrode width  $b$  ( $b_2$  in Fig. 9), leads to a bifurcation point in Fig. 9 above  $K_{Ic}^2$  and thereby to crack deflection during the first unstable stage (see Section 3.3.2). In the experiments, the case where the crack is straight in the first unstable stage and then deflects under increasing load is not encountered.

This simple model of the quasi-static stress intensity factors provides an understanding for the qualitatively different crack paths (straight and deflected) depending on electrode width and the stable and unstable stages on these paths. It is similar to one assessing different crack paths in thermal shock cracking (Bahr et al., 1995). The above

qualitative analysis, however, is not able to explain the crack-tip regressing towards the electrode edge in the deflected crack contour and the third additional stable stage for large crack lengths (see Figs. 6 and 7).

## 5. Quantitative fracture mechanics analysis

### 5.1. Finite element modelling

This section provides detailed numerical analysis of the crack propagation and a comparison of numerical results with experiments. The basis of this analysis is again linear-elastic fracture mechanics and criteria (1). Due to the condition  $K_{IV} = 0$ , the effect of electric field is equivalent to the one of thermal expansion in the electrode region. The thermoelastic stress-free strains as driving force for crack propagation are the incompatible strains and can be calculated from the measured displacements (Fig. 4). They are assumed to be homogeneous, even if a crack passes the electrode and unloads the adjacent region. This unloading zone is estimated to be comparable with the electrode width  $b$  which is much smaller than  $L$  (Fig. 1).

A numerical thermomechanical analysis is carried out with the finite element method for the finite specimen. A plane stress model of isoparametric biquadratic elements with quarter-point nodes in the vicinity of the crack tip is used in the FE-code ANSYS<sup>®</sup> (1998) ANSYS Revision 5.5.3, 1998. The material in the electrode region is considered to be completely poled and transversely isotropic (Young's modulus  $E_{11} = E_{22} = 59.5$  GPa and Poisson ratio  $\nu_{12} = 0.34$ ). The material in the inactive zone is isotropic ( $E_{\text{iso}} = 66.5$  GPa,  $\nu = 0.37$ ). The mismatch zone between the active and the inactive zone is estimated as half the specimen thickness and is not considered in our analysis because of the very thin plate geometry. The stress intensity factors  $K_I$  and  $K_{II}$  are determined from the displacements and from the stresses in the vicinity of the crack tip according to linear fracture mechanics.

The stress distribution in the finite samples without crack shows two differences in comparison to the semi-infinite plate (Fig. 10): the magnitude of the tensile stresses decreases and the compressive stresses next to the electrode increase with increasing electrode coverage  $b/W$  (Fig. 1). In Fig. 10, the stress is normalised by the product of the elastic modulus  $E_{22}$  and the arbitrarily chosen stress-free strain  $\varepsilon_{22}$  in  $x_2$ -direction. In plane stress the results do not depend on the Poisson ratio.

### 5.2. Stress intensity for a straight crack

In contrast to the semi-infinite specimen, the stress distribution yields significantly smaller  $K_I$  for a straight crack in a finite specimen, particularly next to the electrode as consequence of the compressive stresses in this zone (Fig. 11). Another deviation to Figs. 8 and 9 is the asymptotic behaviour of the stress intensity factor for  $a/b \rightarrow 1$  because of different materials on both sides (Zak-Williams singularity for  $a/b = 1$ , Hutchinson and Suo, 1992, p. 131). However, this latter behaviour has no significant consequence for crack propagation.

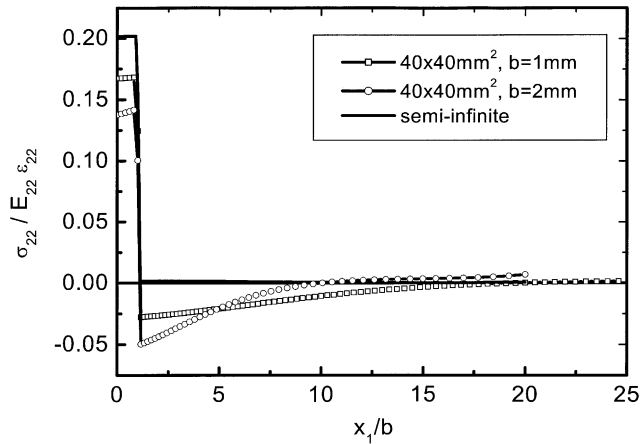


Fig. 10. Stresses due to strain incompatibility for a real specimen as compared to an idealised semi-infinite specimen without crack.

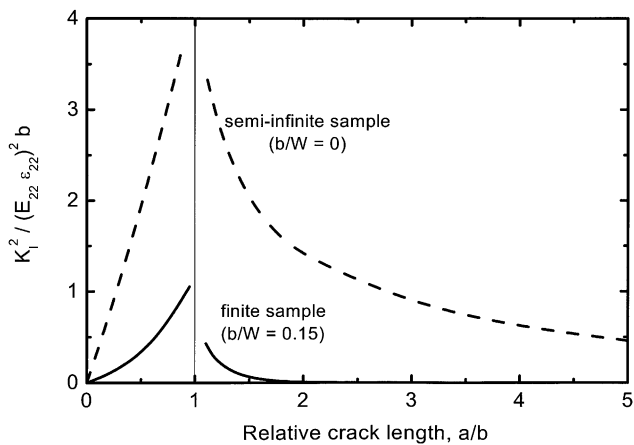


Fig. 11. Squared normalised mode I stress intensity factor as calculated by FEM along the crack path for the straight crack in a semi-infinite specimen and in a finite specimen.

As a result of these effects in a finite body, the straight crack propagation with three stages is identical as discussed in Section 4, but shifted towards higher electric fields. More interesting is the curved crack propagation which we analyse in the next section.

### 5.3. Curved crack simulation

The path of a curved non-kinked crack can be calculated from the local symmetry condition  $K_{II} = 0$  in Eq. (1). Several numerical methods have been proposed for crack path determination using FEM:

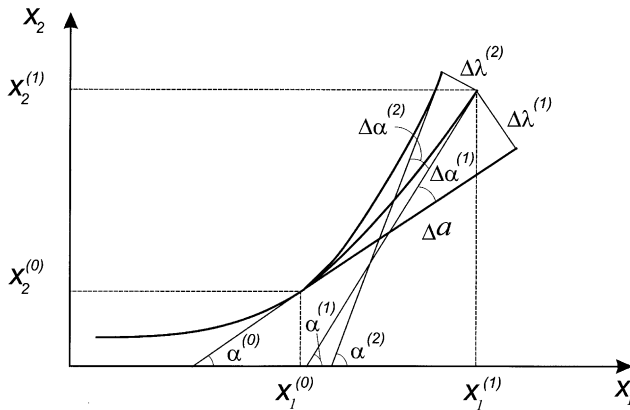


Fig. 12. Iteration method for incremental simulation of propagation of a curved crack.

(a) Methods based on the crack path prediction as incremental straight crack extension with a direction angle change calculated from the current crack closure integrals (Herrmann and Grebner, 1984; Herrmann and Dong, 1992) or from the current stress intensity factor-ratio  $K_{II}/K_I$  (e.g. Bahr et al., 1995; Gunnars et al., 1997).

(b) Methods based on the crack path prediction as incremental curved extensions (Sumi, 1985). Starting from the first-order perturbation solution, the stress intensity factors along a slightly curved crack are resolved as analytical terms of arbitrary crack shape parameters and pre-existing crack-tip stress field. The crack path extension results from the crack shape parameters fulfilling the local symmetry condition  $K_{II} = 0$ . This method requires knowledge of the correction factors representing the effect of stress redistribution due to crack growth in a finite body.

Theilig (1997) avoids this by additionally calculating the stress intensity factors for a straight crack extension increment and by comparing them with the stress intensity factors of the curved crack extension increment which fulfills the local symmetry condition. This leads to the curved crack path parameters from the stress intensity factors of the crack with the straight extension.

These predictions provide only good results for extensions of slightly curved cracks due to their derivation from a perturbation solution of first order. Applying these methods to our problem, the simulated crack path always drifts from the experimental contour, especially in the strongly curved region (Fig. 6), even in the case of very small crack increments. Another disadvantage of these prediction methods lies in the accumulation of errors with progressive increments, so that errors in early increments have decisive implications for the divergence of the crack contour in the following crack propagation.

Therefore, an iterative incremental technique for the crack propagation simulation is proposed. Fig. 12 illustrates the iteration procedure for a crack growth increment  $\Delta a$ :

$$\Delta\lambda^{(i)} = -\frac{K_{II}^{(i)}}{K_I^{(i)}}\Delta a,$$

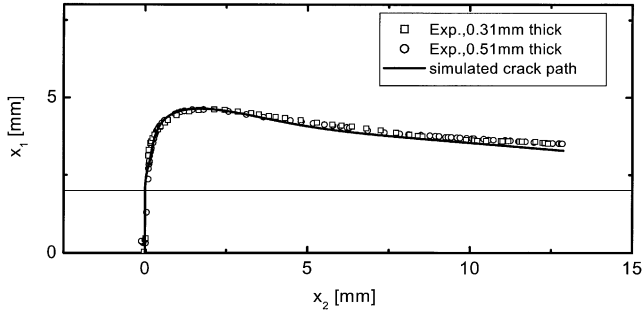


Fig. 13. Comparison of the experimentally and theoretically determined curved crack paths.

$$\begin{aligned} \Delta\alpha^{(i)} &= -2 \frac{K_{II}^{(i)}}{K_I^{(i)}}, \\ \alpha^{(i)} &= \alpha^{(i-1)} + \Delta\alpha^{(i)}, \\ x_1^{(i)} &= x_1^{(i-1)} - \Delta\lambda^{(i)} \sin \alpha^{(i)}, \\ x_2^{(i)} &= x_2^{(i-1)} + \Delta\lambda^{(i)} \cos \alpha^{(i)}. \end{aligned} \tag{2}$$

In Fig. 12, the upper index (0) provides the co-ordinates  $x_1^{(0)}$ ,  $x_2^{(0)}$  and tangent angle  $\alpha^{(0)}$  at the tip of a pre-existing crack fulfilling the local symmetry condition. Index (i) describes the iteration step (i). In iteration step (1), the pre-existing crack is extended straight by  $\Delta a$  in the tangential direction  $\alpha^{(0)}$  at the crack tip. In the subsequent steps the crack extension is adjusted by quadratic splines. In every step an FE-analysis is performed to calculate the stress intensity factors  $K_I$  and  $K_{II}$  thereby providing the corrections  $\Delta\lambda^{(i)}$  and  $\Delta\alpha^{(i)}$  according to the procedure given in (2). The first iteration step is the result of the prediction method (Theilig, 1997). The iteration is ended once the following condition is met:

$$\left| \frac{K_{II}^{(i)}}{K_I^{(i)}} \right| \leq \varepsilon. \tag{3}$$

The co-ordinates  $x_1^{(i)}$ ,  $x_2^{(i)}$  and the tangent angle  $\alpha^{(i)}$  are the starting point for the next crack growth increment.

In our simulation we chose  $\varepsilon = 10^{-3}$ . In slightly curved pieces of the crack contour only one iteration is necessary for  $\Delta a = 0.1$  mm, while in the deflected regime it requires 2 to 3 iterations for  $\Delta a = 0.05$  mm. This confirms that the prediction methods alone are not suitable for a strongly curved crack.

The simulated and experimental crack contour almost coincide, even in the very strongly curved region (Fig. 13). The negligible deviation in the second unstable stage and thereafter may be ascribed to dynamic effects which are not considered in our analysis.

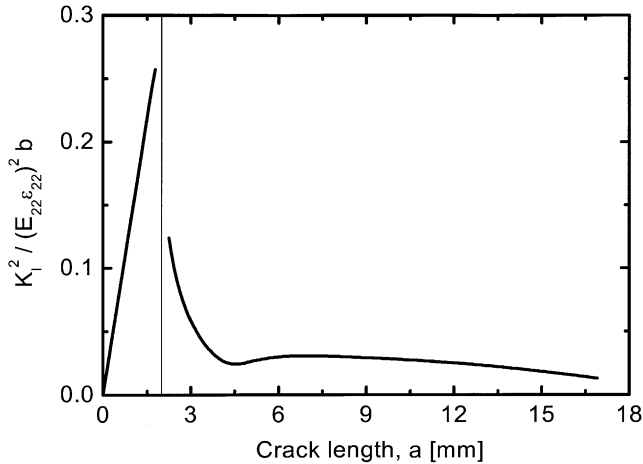


Fig. 14. Squared normalised mode I stress intensity factor as calculated by FEM along the path for the curved crack.

#### 5.4. Determination of crack extension

The  $K_I$ -curve as a function of the crack length in Fig. 14 calculated in the simulation is utilised as the basis for the crack length determination. Comparing with Fig. 8 it is apparent that the second unstable stage and the subsequent stable stage are caused by the minimum of  $K_I$  at  $a = 4.55$  mm and the following increase and decrease. This is a consequence of the compressive stresses behind the electrode edge (Fig. 10) and boundary effects in the finite sample.

The curved crack propagation depending on the electric field  $E$  can be discussed by means of the  $K_I$ -curve. In the upper half of Fig. 15, the curves denoted by  $E_0$  to  $E_3$  are the stress intensity factors  $K_I$  for a crack of length  $a$  under the electric field  $E_0$  to  $E_3$ , respectively. The electric field increases with larger index. Dashed and solid arrows describe stable and unstable crack propagation, respectively.

The scenario for the propagation of a deflected crack can now be derived from this diagram as follows: An initial crack  $a_0$  starts at  $E_0$  due to (1)  $K_I = K_{Ic}$  (corresponding to  $a$  starting value of the  $R$ -curve for poled material) and grows stably ( $dK_I/da < dK_R/da$ ) up to  $E_1$  because of its developing process zone. At  $E_1$  the condition  $dK_I/da \geq dK_R/da$  is met the first time and the crack will propagate unstable.

Quantification of the first stage of stable crack propagation would require a set of  $R$ -curves for different applied electric fields. As these measurements are not available, we only start with modelling the more interesting first unstable stage by adopting the experimental average values  $E_1 = 1.0$  kV/mm and  $a_1 = 0.55$  mm (Section 3.3.2). This unstable stage will end at  $a_2$ , where  $K_I = K_{R\text{-plateau}}$  (for unpoled material) is met on the downward slope of the  $E_1$ -curve. An increase of the electric field leads to a stable crack regime corresponding to the dashed arrows up to  $E_2$ , where the minimum of the  $E_2$ -curve at  $a_3 = 4.45$  mm is equal to the  $K_{R\text{-plateau}}$  (for unpoled material). At this

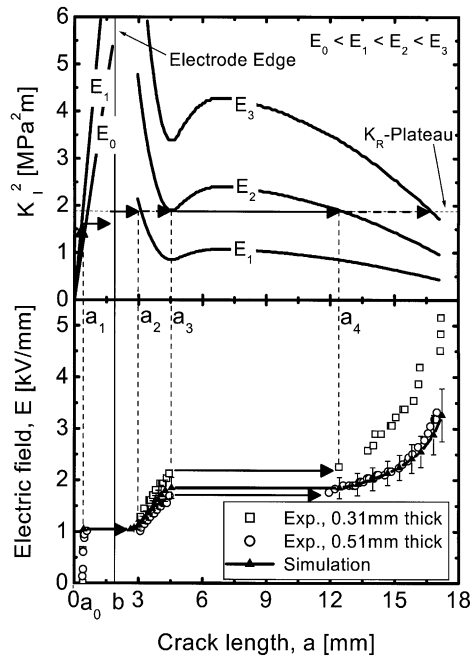


Fig. 15. Fracture mechanics analysis of the propagation for the curved crack depending on the electric field. Upper half: Squared mode I stress intensity factor for different electric fields. The regions of stable and unstable crack propagation are indicated by dashed and solid arrows, respectively. Lower Half: Comparison of the experimentally measured and theoretically determined crack length depending on the electric field.

electric field, the crack will jump to  $a_4 = 12.45$  mm. It is worth noting that the jump from  $a_3$  to  $a_4$  and the values  $a_3$  and  $a_4$  derived from the  $K_I$ -curve above are quite independent of the  $K_{R\text{-plateau}}$  value. After this second unstable stage, only stable crack growth is possible with a further increase of the electric field.

Accordingly, the five stable and unstable stages of crack propagation as observed in the experiments (see Section 3.3.2) are completely constructed and are provided in Fig. 15. The characteristic lengths  $a_3$  and  $a_4$  have also been computed without the knowledge of the load and the  $K_{R\text{-plateau}}$  value.

For determination of  $E_2$  to  $E_4$  and of the crack length as a function of the electric field (lower half of Fig. 15) the  $K_{R\text{-plateau}}$  value of the unpoled material (Fig. 3) and the incompatible strains depending on the electric field are required. The incompatible strains consisting of ferroelectric, ferroelastic and piezoelectric strain can also be understood as the difference between total and elastic strain and can be calculated from the measured displacements in Fig. 4. The proportionality factor between the incompatible strains and the displacements has been obtained by means of an FE calculation. As mentioned in Section 3.2, these displacements could be measured only up to  $E = 1.9$  kV/mm in the clamped specimens. For very high electric fields ( $E > 3$  kV/mm), they are assumed to be the same as in a free completely poled sample and for electric fields between 1.9 and 3 kV/mm, an interpolation between these two curves

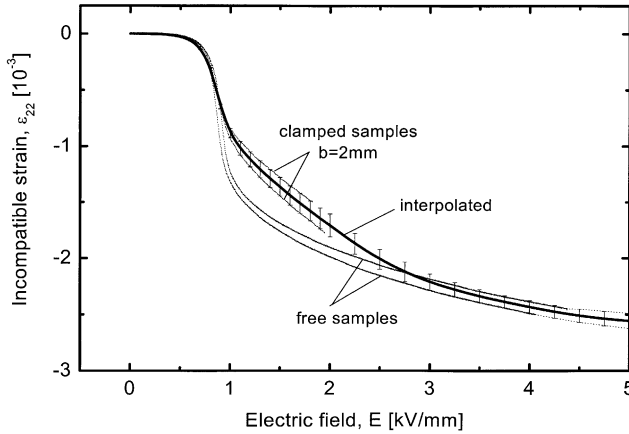


Fig. 16. Calculated and interpolated incompatible strains depending on the electric field as computed from displacement measurements.

(see Fig. 16) is applied. In this figure, the calculated incompatible strain vs. electric field is plotted including scatter due to the variation of the two displacement measurements (Fig. 4).

In the lower half of Fig. 15 the simulated crack length depending on the electric field is compared with the experiment. The agreement is excellent with respect to the transitions between stable and unstable stages. The computed crack length as a function of the electric field exhibits some variability due to scatter in the incompatible strains (Fig. 16) and the plateau values in the  $R$ -curves (Fig. 3). The simulated curve lies closer to the experimental curve with specimen width of 0.51 mm, with increasing deviation for higher electric fields. The latter is attributed to two effects. First, the formation of secondary cracks at the electrode edge at higher electric fields. These then can unload the main crack, which in turn requires higher strains and, therefore, higher electric fields for the same crack driving force. Second, for high electric fields, the stress-free strains represent the lower limit of the incompatible strains in Fig. 16, because poling in  $x_3$ -direction is reduced by tensile mechanical stresses  $\sigma_{22}$ .

## 6. Discussion

We have provided a novel experiment, which allows controlled study of crack propagation due to strain incompatibility. It supplements and draws from prior work on thermal shock and crack propagation under thermal shock conditions (Bahr et al., 1995). As in thermal shock, propagation of straight cracks and deflected cracks is observed with the attendant transition between both modes. Starting with a highly defined pre-crack and using the electric field as a means of providing strain incompatibility affords superior control over crack propagation and detailed observation of incremental crack growth in the optical microscope.

The wealth of material behaviour of the utilised ceramic includes a ferroelectric, piezoelectric and ferroelastic response. Piezoelectricity yields straining under electric field, which, in conjunction with the ferroelectric and ferroelastic switching provides strain incompatibility.

Utilisation of a ferroelectric material to provide the electric field generated strain incompatibility, however, also generates some complications. Careful choice of specimen dimensions and measurement procedure reduced the observed complicating issues to small effects as proven in Figs. 13 and 15.

The non-homogeneous electric field at the electrode edge is problematic in two ways. An electric field singularity is located under the electrode edge which due to piezoelectric coupling and ferroelectric switching gives rise to locally increased tensile stresses and leads to the formation of secondary cracks along the electrode edge. These cracks observed at higher electric fields can shield the main crack which thus requires higher strains and higher electric fields. The density of secondary cracks is strongly reduced if the thinnest feasible specimens are selected (dos Santos e Lucato et al., 2001). Furthermore, the electric field incorporates a fringing field next to the electrode edge, providing a volume between active and inactive material with ill-defined material properties and a highly non-homogenous stress field due to the electro-mechanical coupling in ferroelectrics. As mentioned in Section 5.1, this region is neglected in our modelling.

As both secondary cracking and lateral extension of the fringing field could be reduced by utilising the thinnest specimens possible, very thin plates of 0.5 mm were chosen. A slight drawback with this choice lay in the fact that in this thickness regime there is a slight variation of  $R$ -curve with specimen thickness as ferroelastic toughening depends on the macroscopic stress state (plane stress or plane strain) and the  $R$ -curve therefore depends on specimen thickness (dos Santos e Lucato et al., 2002). Measuring the  $R$ -curve with plates of 1mm thickness which is the thinnest possible for mechanical loading in our equipment, proved to be the best possible compromise. The thickness dependence of the  $R$ -curve can contribute to the experimental scattering in the electric field in Fig. 7.

Another issue arises from the crack growth velocity. Ferroelastic behaviour leads to domain switching under the influence of the crack tip stress field, thereby setting up a process zone and providing crack toughening due to crack tip shielding. The amount of shielding again depends on the crack growth velocity. This effect was accounted for by obtaining  $R$ -curves on our specimens with controlled crack velocity and by obtaining the crack tip position after some waiting time with the electrically driven crack measurement. With respect to crack velocity, only the toughening effect and therefore the plateau value of an unstably grown crack could not be fully assessed. Work by Glazounov et al. (2001), however, showed in X-ray diffraction studies, that domain switching occurs even under the conditions of unstable crack growth. Given the very good agreement of the simulation with the experiment in the unstable crack growth regimes, it can be concluded that a significant amount of toughening is obtained up to very high crack growth velocities.

In summary, the results of the fracture mechanics analysis show a very good quantitative agreement with the experiments in the crack contours, in the stages of crack

propagation and the transitions between them and also in the crack length as a function of the electric field. This confirms that the unstable crack propagation can be described sufficiently with the static fields used in the analysis.

The same experimental set-up with in-plane prepoled specimens is currently being used to study the effect of  $K_{IV}$  on the crack path and on the fracture criterion for piezoelectric material  $f(K_I, K_{IV}) = 0$ , which will be the subject of a forthcoming publication.

## 7. Conclusion

The following results have been obtained from the present study:

- Different crack types are achievable by variation of geometric conditions. The crack paths are reproducible with very high accuracy.
- Small electrodes lead to straight cracks with two transitions between stable and unstable crack growth regions, while large electrodes result in curved cracks with four transitions.
- An iteration method is proposed to simulate the propagation of curved cracks also for the case of a strong crack curvature.
- Fracture mechanics analysis is able to explain the different paths of cracks depending on the electrode width  $b$  and the stable and unstable crack growth stages with their transitions on these paths.

## Acknowledgements

The authors gratefully acknowledge the support of this work by the Deutsche Forschungsgemeinschaft (DFG) under contract No. Rö 954/13 and Ba 1561/3.

## References

- Aburatani, H., Harada, S., Uchino, K., Furuta, A., Fuda, Y., 1994. Destruction mechanisms in ceramic multilayer actuators. *Jpn. J. Appl. Phys.* 33, 3091–3094.
- ANSYS Revision 5.5.3, 1998. Swanson Analysis Systems Inc., Houston, USA.
- ASTM, 1996. Standard test method for plane strain fracture toughness of metallic materials, E399-90. In: *Annual Book of ASTM standards*, vol. 3.03. pp. 407–437.
- Bahr, H.-A., Bahr, U., Gerbatsch, A., Pflugbeil, I., Vojta, A., Weiss, H.-J., 1995. Fracture mechanical analysis of morphological transitions in thermal shock cracking. In: Bradt, R.C., Hasselman, D.P.H., Munz, D., Sakai, M., Shevchenko, V.Y. (Eds.), *Fracture Mechanics of Ceramics*, vol. 11. Plenum Press, New York and London, pp. 507–522.
- Cotterell, B., Rice, J.R., 1980. Slightly curved or kinked cracks. *Int. J. Fract.* 16, 155–169.
- dos Santos e Lucato, S.L., Lupascu, D.C., Kamlah, M., Rödel, J., Lynch, C.S., 2001. Constraint-induced crack initiation at electrode edges in piezoelectric ceramics. *Acta Mater.* 49, 2751–2759.
- dos Santos e Lucato, S.L., Lindner, J., Lupascu, D.C., Rödel, J., 2002. Influence of the electrical and geometrical boundary conditions on crack growth in PZT. *Key Eng. Mater.* 206–213, 609–612.
- Furuta, A., Uchino, K., 1993. Dynamic observation of crack propagation in piezoelectric multilayer actuators. *J. Am. Ceram. Soc.* 76, 1615–1617.

- Glazounov, A.E., Fett, T., Reszat, J.-Th., Hoffmann, M.J., Munz, D., Wroblewski, T., 2001. Influence of domain switching state on *R*-curves interpreted by using X-ray diffraction. *J. Mater. Sci. Lett.* 20, 877–880.
- Gunnars, J., Stähle, P., Wang, T.C., 1997. On crack path stability in a layered material. *Comput. Mech.* 19, 545–552.
- Haertling, G.H., 1999. Ferroelectric ceramics: history and technology *J. Am. Ceram. Soc.* 82, 797–818.
- Herrmann, K.P., Dong, M., 1992. Thermal cracking of two-phase composite structures under uniform and non-uniform temperature distribution. *Int. J. Solids Struct.* 29, 1789–1812.
- Herrmann, K.P., Grebner, H., 1984. Curved thermal crack growth in nonhomogeneous materials with different shaped external boundaries I. theoretical results. *Theor. Appl. Fract. Mech.* 2, 133–146.
- Hutchinson, J.W., Suo, Z., 1992. Mixed mode cracking in layered materials. *Adv. Appl. Mech.* 29, 63–91.
- Rödel, J., Kelly, J.F., Lawn, B.R., 1990. In situ measurement of bridged crack interfaces in the scanning electron microscope. *J. Am. Ceram. Soc.* 73, 3313–3318.
- Schneider, G.A., Rostek, A., Zickgraf, B., Aldinger, F., 1995. Crack growth in ferroelectric ceramics under mechanical and electrical loading. *Electroceramics IV*, Augustinus Buchhandlung, Aachen, ed. 1, 1211–1216.
- Schneider, G.A., Weitzing, H., Zickgraf, B., 1996. Crack growth in ferroelectric ceramics and actuators under mechanical and electrical loading. *Frac. Mech. Ceram.* 12, 149–160.
- Sumi, Y., 1985. Computational crack path prediction. *Theor. Appl. Fract. Mech.* 4, 149–156.
- Suo, Z., Kuo, C.-M., Barnett, D.M., Willis, J.R., 1992. Fracture mechanics for piezoelectric ceramics. *J. Mech. Phys. Solids* 40, 739–765.
- Takahashi, S., Ochi, A., Yonezawa, M., Yano, T., Hamatsuki, T., Fukui, I., 1983. Internal electrode piezoelectric ceramic actuator. *Ferroelectrics* 50, 181–190.
- Theilig, H., 1997. A higher order fatigue crack paths simulation by the MVCCI-method. In: *Advances in Fracture Research, Proceeding of the Ninth ICF*, Australia, pp. 2235–2243.
- Uchino, K., 1997. *Piezoelectric Actuators and Ultrasonic Motors*. Kluwer Academic Publishers, Boston.



## Erratum

Erratum to “Electrically driven cracks in piezoelectric ceramics: experiments and fracture mechanics analysis”, *Journal of the Mechanics and Physics of Solids* 50 (2002) 2333–2353<sup>☆</sup>S.L. dos Santos e Lucato<sup>a</sup>, H.-A. Bahr<sup>b</sup>, V.-B. Pham<sup>b</sup>,  
D.C. Lupascu<sup>a</sup>, H. Balke<sup>b</sup>, J. Rödel<sup>a,\*</sup>, U. Bahr<sup>c</sup><sup>a</sup>Darmstadt University of Technology, Institute of Materials Science, Ceramics Group, Petersenstr. 23, 64287 Darmstadt, Germany<sup>b</sup>Dresden University of Technology, Institute of Solid Mechanics, 01062 Dresden, Germany<sup>c</sup>Dresden University of Technology, Institute of Theoretical Physics, 01062 Dresden, Germany

Unfortunately an error occurred in the scaling of Fig. 10 in our paper “Electrically driven cracks in piezoelectric ceramics: experiments and fracture mechanics analysis”, *Journal of the Mechanics and Physics of Solids* 50 (2002) 2333–2353. The corrected figure is as follows:

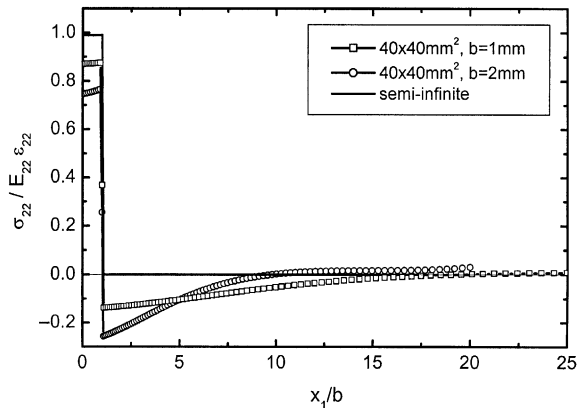


Fig. 10. Stresses due to strain incompatibility for a real specimen as compared to an idealised semi-infinite specimen without crack.

<sup>☆</sup> PII of the original article: S0022-5096(02)00030-3

\* Corresponding author. Tel.: +49-6151-166316; fax: +49-6151-166314.

E-mail address: roedel@ceramics.tu-darmstadt.de (J. Rödel).